Check for updates

View Article Online
View Journal

# Energy Advances

## Accepted Manuscript

This article can be cited before page numbers have been issued, to do this please use: O. A. Alvarez, C. Da Silva and C. H. Amon, *Energy Adv.*, 2026, DOI: 10.1039/D6YA00018E.


This is an Accepted Manuscript, which has been through the Royal Society of Chemistry peer review process and has been accepted for publication.

Accepted Manuscripts are published online shortly after acceptance, before technical editing, formatting and proof reading. Using this free service, authors can make their results available to the community, in citable form, before we publish the edited article. We will replace this Accepted Manuscript with the edited and formatted Advance Article as soon as it is available.

You can find more information about Accepted Manuscripts in the Information for Authors.

Please note that technical editing may introduce minor changes to the text and/or graphics, which may alter content. The journal's standard Terms & Conditions and the Ethical guidelines still apply. In no event shall the Royal Society of Chemistry be held responsible for any errors or omissions in this Accepted Manuscript or any consequences arising from the use of any information it contains.

ROYAL SOCIETY OF CHEMISTRY

rsc.li/energy-advances

View Article Online
DOI: 10.1039/D6YA00018E

# A 3D Electrochemical-Thermal Coupled Model for Pouch-Type Lithium-ion Batteries with Counter-Tab Configuration

Oscar A. Alvarez[1], Carlos M. Da Silva[1], Cristina H. Amon[1,2*]

[1] Department of Mechanical and Industrial Engineering, University of Toronto, Toronto, ON, M5S3G8, Canada

[2] Department of Chemical Engineering and Applied Chemistry, University of Toronto, Toronto, ON, M5S3E5, Canada

*Corresponding Author: cristina.amon@utoronto.ca

Open Access Article. Published on 10 June 2026. Downloaded on 6/18/2026 2:09:24 PM.
This article is licensed under a Creative Commons Attribution-NonCommercial 3.0 Unported Licence.

## Abstract

Lithium-ion batteries (LIBs) are the dominant energy source for electric vehicles (EVs) and battery energy storage systems (BESS) owing to their superior performance compared to other storage technologies. However, thermal management remains a critical challenge, as LIBs must operate within a tight temperature range (typically 25-40ºC) and maintain spatial temperature uniformity (ideally <5ºC). Emerging large-format (>50 Ah) LIB pouch cells are particularly susceptible to spatially non-uniform heat generation driven by higher current densities near their tabs, resulting in significant temperature gradients that compromise both performance and lifetime. This work presents a novel three-dimensional electrochemical-thermal (ECT) coupled model that addresses the limitations of existing ECT models in accurately predicting spatial temperature gradients across different C-rates, particularly in large-format pouch cells with counter-tab configurations that exhibit two hot spots near the cell opposite tabs. By incorporating a heat-generation distribution factor, this ECT model captures non-uniform Joule heating arising from distributed current density in the cell metal current collectors, in turn enabling accurate predictions of spatio-temporal temperatures in these large-format pouch cells. Experimental validation through voltage and temperature measurements confirms the accuracy and robustness of the proposed model, demonstrating its ability to predict the thermal characteristics of large-format pouch cells, which are increasingly adopted in EVs and BESS. The validated model is employed to conduct a comprehensive sensitivity analysis to examine how variations in electrode layer properties influence the magnitude of volumetric heat generation rate, and the role of tab geometry in controlling its spatial distribution.

Keywords: Electrochemical-thermal coupled model, non-uniform heat generation in Lithium-ion pouch cells, temperature gradients in Lithium-ion battery cells.

## 1. Introduction

Lithium-ion batteries (LIBs) are playing a crucial role in transportation electrification, being the preferred energy source for electric vehicles (EVs) and battery energy storage systems (BESS) due to their high energy and power densities, high-voltage capability, and low self-discharge [1,2]. LIB cells must work within a tight temperature range (25-40ºC) and maintain spatial temperature uniformity (below 5ºC) across large battery packs to ensure optimal performance and lifespan. Since LIB cells generate heat during both charging and discharging processes, battery thermal management systems (BTMS) are essential for maintaining suitable thermal conditions [3].

Accurate LIB temperature field prediction, especially identifying hot spots in large-format (> 50 Ah) pouch cells, is critical for achieving effective BTMS designs targeting localized heat dissipation [4,5]. The spatial temperature distribution in large-format LIB pouch cells that are emerging in EVs is highly influenced by their spatially non-uniform heat generation and anisotropic thermophysical properties. Anisotropic heat conduction arises from the internal layered structure of LIB pouch cells, which leads to different effective thermal conductivities parallel ($k_{eff}$

Energy Advances Accepted Manuscript

View Article Online
DOI: 10.1039/D6YA00018E

Open Access Article. Published on 10 June 2026. Downloaded on 6/18/2026 2:09:24 PM.
This article is licensed under a Creative Commons Attribution-NonCommercial 3.0 Unported Licence.

$_{\text{in-plane}}$) and perpendicular ($k_{\text{eff cross-plane}}$) to the electrode layers. Several methods have been developed to estimate these effective thermophysical properties, including our prior experimental-numerical inverse heat transfer (IHT) techniques [6,7,8], steady-state experiments [9,10], equivalent thermal circuit approaches based on the electrode layers specifications [11,12], and multi-length-scale thermal modeling frameworks [13]. On the other hand, an accurate estimation of the distributed heat generation across large-format pouch cells is equally essential for high-fidelity thermal modeling and BTMS design.

Equivalent circuit models (ECMs) are commonly used to describe the electrical behavior of LIBs through resistor-capacitor networks, significantly simplifying their complex electrochemical processes [14]. When coupled with thermal models, ECMs provide overall heat generation rate inputs to predict average cell temperatures, in some cases, with thermal feedback loops used to update the ECM parameters. Notable examples from the literature include Estevez et al. [15], Tang et al. [16], and Wang et al. [17] for pouch cells, and Palmieri et al. [18] for cylindrical cells. However, a fundamental drawback of ECM-based thermal models is their inability to capture the spatially non-uniform heat generation, particularly the localized Joule heating caused by current density concentration near the tabs of large-format pouch cells operating at high C-rates. By treating the cell as a lumped thermal system, standard ECMs cannot resolve localized hot spots that are critical for BTMS design. To enhance spatial resolution, Zhao et al.[19] developed an electro-thermal ECM that accounted for thermal transport across the cell length and thickness. While this approach improved the resolution of through-thickness temperature gradients, it neglected temperature variations across the cell width. Furthermore, because ECMs have inherent fidelity limitations and cannot evaluate electrode-level electrochemical performance, determining ECM parameters requires extensive preliminary experimental testing and optimization.

High-fidelity electrochemical-thermal (ECT) coupled models primarily rely on pseudo-two-dimensional (P2D) models to resolve sub-cell internal processes, addressing the limitations of simpler ECM-based approaches. P2D models specifically account for conservation of mass and charge, resolving the electrochemical processes along a single, one-dimensional (1D) thickness direction within a sub-cell [20]. While the standard P2D model operates in 1D, extensions to two-dimensional (2D) and three-dimensional (3D) domains are employed to capture the spatial distribution of electrochemical processes. Critically, P2D models facilitate the development of ECT coupled models by being linked with thermal models across two distinct length scales. These coupled models typically involve two domains: one dedicated to electrochemical processes (1D, 2D, or 3D at the sub-cell level), and another focused on thermal transport (1D, 2D or 3D at the cell level). Model complexity naturally scales with the dimensionality of each domain. For instance, Wang et al. [21] coupled a 1D P2D model with a 3D thermal model for cylindrical cells, sharing averaged volumetric heat generation rate and temperature between the domains. In a similar work by Li et al. [22], 3D sub-cell and cell domains shared average information of volumetric heat generation rate and temperature. An et al. [23] analyzed a 1D P2D model in conjunction with a 1D thermal model for a LIB pouch cell, examining

Energy Advances Accepted Manuscript

View Article Online
DOI: 10.1039/D6YA00018E

Open Access Article. Published on 10 June 2026. Downloaded on 6/18/2026 2:09:24 PM.
This article is licensed under a Creative Commons Attribution-NonCommercial 3.0 Unported Licence.

temperature gradients across its thickness direction. He et al. [24] developed a more advanced ECT model for lithium-iron-phosphate (LFP)-based pouch cells with adjacent-tab configuration, employing a plane-projection method to transfer spatial volumetric heat generation rate from a sub-cell to a cell domain, and transferring temperature information back from the cell to sub-cell domain. Lin et al.[25] followed a similar approach for LFP cells at C-rates as high as 5C discharge. Other studies have leveraged ECT models to refine cell-tab design and geometry. Samba et al.[26] developed an ECT model applied to a unique 2D sub-cell domain to evaluate tab-induced temperature gradients, without characterization of through-thickness cell thermal behavior. In a related study, Moayedi et al.[27] used the Newman-Tiedemann-Gu-Kim (NTGK) empirical model to assess the impact of aspect ratios on cell thermal uniformity, while disregarding the anisotropic thermal properties of the electrode stack. Optimization efforts by Zhang et al.[28] and Mastali et al.[29] have transitioned toward sub-cell to cell, 1D-2D and 1D-3D coupled models, respectively. These models provide significant computational efficiency for tab layout analysis.

While advanced ECT models – particularly those utilizing the plane-projection method – have successfully predicted cell-average temperature and minor temperature gradients for C-rates as high as 5C, their accuracy in resolving spatial temperature gradients diminishes significantly for large-format pouch cells with a counter-tab configuration operating across various C-rates. This is a critical gap, as these cells are increasingly used in EV applications and exhibit distinct temperature gradients compared to adjacent-tab layouts. While cells with adjacent-tab configurations typically manifest a single concentrated hot spot near the tabs, cells with counter-tab configuration result in the formation of two distinct hot spots at opposite ends of the cell. This bifurcation of heat concentration leads to more complex spatial temperature gradients that current models fail to capture. Therefore, there is a clear need to develop high-fidelity ECT models capable of resolving these thermal profiles in emerging large-format pouch cells across a wide range of C-rate levels.

To accurately estimate the temperature field in large-format LIB pouch cells, this study proposes an ECT coupled model that addresses the need for higher-fidelity representations that explicitly account for anisotropic thermal conductivity and detailed 3D heat-generation distributions. Unlike previous ECT coupled models that project plane-distributed volumetric heat generation rate from sub-cell to cell domains [24,25], the ECT model developed in this work introduces a novel heat-generation distribution factor strategy based on dominant resistive (Joule) heating processes through the cell current collectors. This strategy enables accurate prediction of 3D spatial temperature gradients in industry-relevant LIB pouch cells with counter-tab configuration operating at different levels of C-rate. Experimental validation of both voltage responses and cell surface temperatures is provided in this study.

The structure of the remainder of this manuscript is as follows. Section 2 establishes the theoretical basis by describing our ECT model, focusing on the numerical domains and governing equations. Section 3 introduces the LIB pouch cell – with nickel manganese cobalt cathode – that is the subject of this analysis. The details of the

Energy Advances Accepted Manuscript

View Article Online
DOI: 10.1039/D6YA00018E

Open Access Article. Published on 10 June 2026. Downloaded on 6/18/2026 2:09:24 PM.
This article is licensed under a Creative Commons Attribution-NonCommercial 3.0 Unported Licence.

experimental setup are provided in Section 4, followed by Section 5, which presents and compares the experimental measurements against the numerical predictions. Section 6 then focuses on a comprehensive parametric analysis to assess the impact of sub-cell electrode and tab parameters on the cell thermal response. Section 7 summarizes the key findings and contributions of the present study.

## 2. Three-dimensional electrochemical-thermal coupled model

This work proposes a novel three-dimensional electrochemical-thermal (ECT) coupled model, referred to hereafter as the ECT model, to concurrently predict the electrochemical and thermal dynamics of large-format pouch cells with counter-tab configuration. This ECT model employs a bi-directional coupling between 3D sub-cell and 3D cell domains via a plane-projection scheme, as depicted in Fig. 1. In addition, this model utilizes a distribution factor (df) to ensure precise spatial distribution of the volumetric heat generation rate. While the thermal model resolves conservation of energy across the 3D cell volume, the electrochemical processes are modeled using a physics-based extended P2D model applied to the 3D sub-cell (often referred to as "P4D"), capturing electrochemical variables and their temperature dependencies across the sub-cell thickness, length, and width.

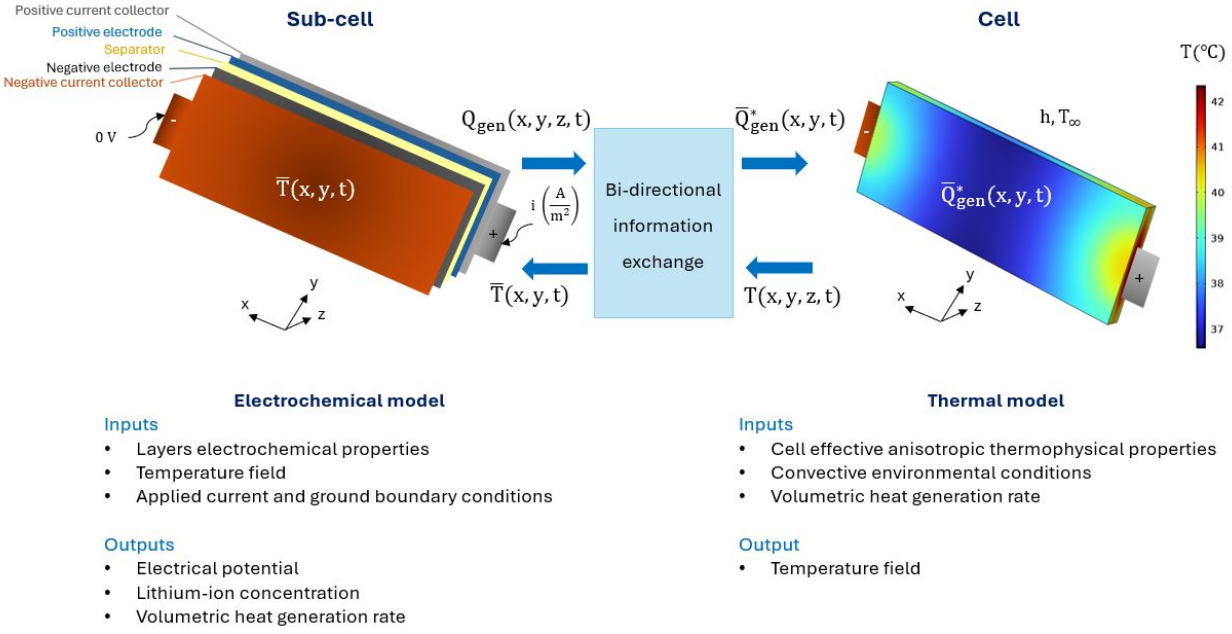


Fig. 1. Three-dimensional electrochemical-thermal (ECT) coupled model, detailing the interacting numerical domains, inputs, outputs, and bi-directional information exchange. The model utilizes a sub-cell domain for calculating electrochemical variables, such as electrical potential, lithium-ion concentration, and volumetric heat generation rate ($Q_{gen}$), and a cell domain for determining cell temperature field (T), where cell tabs are not considered. The coupling is bi-directional: $\overline{Q}^{*}_{gen}$ is projected from the sub-cell domain to the cell domain onto the X-Y plane and a distribution factor (df), and the resulting $\overline{T}$ is projected back to the sub-cell domain onto the X-Y plane.

Energy Advances Accepted Manuscript

View Article Online
DOI: 10.1039/D6YA00018E

Open Access Article. Published on 10 June 2026. Downloaded on 6/18/2026 2:09:24 PM.
This article is licensed under a Creative Commons Attribution-NonCommercial 3.0 Unported Licence.

This approach assumes that electrochemical processes are fully represented within a sub-cell, while the conservation of energy is analyzed over the cell domain. Volumetric heat generation rate is first calculated in the sub-cell and then projected onto the X-Y plane (sub-cell length and width) before being transferred to the cell domain. In the cell domain, temperature fields are computed and subsequently projected back to the sub-cell using a similar X-Y projection and thickness-averaged method, defined in Equation (1), to update the electrochemical processes. The mathematical expressions for these projection schemes are as follows:

$$\overline{T}(x,y,t) = \frac{1}{L_{cell}}\int_0^{L_{cell}} T(x,y,z,t)dz \qquad (1)$$

$$\overline{Q}_{gen}(x,y,t) = \frac{1}{L_{subcell}}\int_0^{L_{subcell}} Q_{gen}(x,y,z,t)dz \qquad (2)$$

$$\overline{Q}^{*}_{gen}(x,y,t) = \overline{Q}_{gen}(x,y,t) \cdot df(x,y,t) \qquad (3)$$

$$df(x,y,t) = \frac{\overline{Q}_{gen\ cc}(x,y,t)}{Q_{gen\ cc\ average}} \qquad (4)$$

$$\overline{Q}_{gen\ cc}(x,y,t) = \frac{1}{L_{cc}}\int_0^{L_{cc}} Q_{gen\ cc}(x,y,z,t)dz \qquad (5)$$

Here, $L_{subcell}$, $L_{cell}$, and $L_{cc}$ represent the thickness of the sub-cell, cell, and current collectors, respectively. As mentioned previously, the expression in Equation (2) for the projected volumetric heat generation rate is able to capture average temperatures and modest temperature gradients for cells with adjacent-tab configuration operating at high C-rates (up to 5C), as presented in [24,25]. However, this capability diminishes at lower C-rates and different tab layouts. This limitation arises from the formulation of Equation (2), where $\overline{Q}_{gen}$ is computed as a thickness-averaged value. This method inherently emphasizes thicker layers and underrepresents thinner ones – particularly the current collectors, which are the thinnest layers but often the most thermally active due to concentrated current density [30,31]. Non-uniform current density within current collectors leads to spatial variations in Joule heating and uneven electrochemical processes in the active electrodes [32]. This work's ECT model proposes a spatio-temporal distribution factor (df(x,y,t)) based on electric current dynamics through the current collectors, which is deemed to predominantly govern the distribution of Joule heating sources across the cell domain. This non-dimensional distribution factor is predicted by modeling the current density distribution within the metallic current collectors. The ECT model then projects this spatio-temporal distribution factor onto the volumetric heat generation rate ($\overline{Q}^{*}_{gen}$), as presented in Equation (3). This distribution factor is defined in Equations (4) and (5), considering a ratio between the projected volumetric heat generation rate in the metallic current collectors ($\overline{Q}_{gen\ cc}$) and the average volumetric heat generation rate ($Q_{gen\ cc\ average}$) in these layers.

### 2.1 Electrochemical model: P2D applied to a 3D sub-cell domain



Energy Advances Accepted Manuscript

View Article Online
DOI: 10.1039/D6YA00018E

Open Access Article. Published on 10 June 2026. Downloaded on 6/18/2026 2:09:24 PM.
This article is licensed under a Creative Commons Attribution-NonCommercial 3.0 Unported Licence.

The electrochemical model accounts for mass conservation (Equations (6) and (7) in Table 1, and Equations (19)-(21) in Table 2), charge conservation (Equations (9)-(11) in Table 1, and Equations (22)-(24) in Table 2), and electrochemical kinetics (Equations (12)-(14) in Table 1) within the sub-cell domain. This model is applied with the following assumptions:

- Active material particles in both positive and negative electrodes are considered homogeneous spheres of uniform size.
- Volume changes in the electrodes during discharge and charge processes are negligible.
- No gas is generated during the discharge and charge processes.
- All side reactions are negligible.
- Potential effects from solid electrolyte interphase (SEI) layers and lithium dendrites are negligible.

The underlying assumptions are consistent with those widely employed in similar P2D models reported in the literature [20,33], and are deemed appropriate for beginning-of-life (BOL) cells operating within relatively safe temperature ranges (15-50ºC). Extension of this model to significantly degraded cells, which falls outside the current investigation scope, would require fundamental adjustments to account for factors such as SEI growth, side reactions, and electrodes volume expansion [34]. A sub-cell is an architecture with porous positive and negative electrodes, separated by a porous separator, all of which are saturated with liquid electrolyte. Consequently, the movement of lithium ions (Li-ions) occurs via the liquid phase between the electrodes and the separator. At the same time, electron propagation occurs through the solid phase of the electrodes and the metallic positive and negative current collectors. The complete set of governing equations and boundary conditions is presented in Tables 1 and 2, respectively. Mass conservation is established using Fick second law of diffusion in spherical coordinates. Charge conservation is modelled using Ohm law for solid-phase electron transport and concentrated solution theory for electrolyte-based ionic transport [24]. For these processes, the model considers the liquid volume fraction for electrolyte diffusivity and ionic conductivity (Equations 8(a) and 8(b) in Table 1), as well as the solid volume fraction for electrode ionic conductivity (Equation 8(c) in Table 1). The total volumetric heat generation rate is predicted from Equations (15)-(18) in Table 1, aggregating ohmic, activation, and reaction sources from each of the sub-cell layers, including those heat sources from positive and negative electrode layers. Note that only ohmic heating sources are considered for the metal current collector layers. While the ECT model can predict individual heat sources for each electrode, this study focuses on the total volumetric heat generation rate, which aligns with the available system-level experimental validation through cell surface temperatures. Moreover, different cell chemistries can be analyzed by simply adjusting the properties of the corresponding electrodes.

Energy Advances Accepted Manuscript

View Article Online
DOI: 10.1039/D6YA00018E

Open Access Article. Published on 10 June 2026. Downloaded on 6/18/2026 2:09:24 PM.
This article is licensed under a Creative Commons Attribution-NonCommercial 3.0 Unported Licence.

Table 1. Summary of governing equations in the electrochemical model.

| Physical meaning | Governing equation | Nº |
|---|---|---|
| Mass conservation, solid phase | $\frac{\partial c_s^{\pm}}{\partial t} = \frac{1}{r^2}\frac{\partial}{\partial r}\left(r^2 D_s^{\pm}\frac{\partial c_s^{\pm}}{\partial r}\right)$ | (6) |
| Mass conservation, liquid phase | $\varepsilon_l \frac{\partial c_l^{\pm}}{\partial t} = \nabla\cdot\left(D_{l\,eff}^{\pm}\nabla c_l^{\pm}\right) + (1-t_+)\frac{a_l i_{loc}}{F}$ | (7) |
| Effective diffusivity and conductivity | $D_{l\,eff} = D_l\varepsilon_l^{1.5}$ (a); $\sigma_{l\,eff} = \sigma_l\varepsilon_l^{1.5}$ (b); $\sigma_{s\,eff} = \sigma_s\varepsilon_s^{1.5}$ (c) | (8) |
| Charge conservation, solid phase | $\nabla\cdot\left(\sigma_{s\,eff}^{\pm}\nabla\emptyset_s^{\pm}\right) = -S_a^{\pm} i_{loc}$ | (9) |
| Charge conservation, liquid phase | $\nabla\cdot\left(-\sigma_{l\,eff}^{\pm}\nabla\emptyset_l^{\pm} + \frac{2RT\sigma_{l\,eff}^{\pm}}{F}\left(1+\frac{\partial \ln f}{\partial \ln c_l^{\pm}}\right)(1-t_+)\nabla \ln c_l^{\pm}\right) = S_a^{\pm} i_{loc}$ | (10) |
| Specific area | $S_a^{\pm} = \frac{3\varepsilon_s^{\pm}}{r_p^{\pm}}$ | (11) |
| Electrochemical kinetics | $i_{loc} = i_o\left(\exp\left(\frac{\alpha_a \eta F}{RT}\right) - \exp\left(-\frac{\alpha_c \eta F}{RT}\right)\right)$ | (12) |
| | $i_0 = F\kappa_i c_s^{\alpha_c}\left(c_{s,max} - c_s\right)^{\alpha_a}\left(\frac{c_l}{c_{l,ref}}\right)^{\alpha_a}$ | (13) |
| | $\eta = \phi_s - \phi_l - V_{eq}$ | (14) |
| Volumetric heat generation rate | $Q_{gen} = Q_{reaction} + Q_{activation} + Q_{ohmic}$ | (15) |
| | $Q_{reaction} = S_a i_{loc} T\frac{\partial E_{eq}}{\partial T}$ | (16) |
| | $Q_{activation} = S_a i_{loc}\eta$ | (17) |
| | $Q_{ohmic} = \sigma_{s\,eff}^{\pm}\nabla\emptyset_s^{\pm}\cdot\nabla\emptyset_s^{\pm} + \left[\sigma_{eff,l}^{\pm}\nabla\emptyset_{l,k} - \frac{2\sigma_{eff,l}^{\pm}RT}{F}\left(1+\frac{\partial \ln f_{\pm}}{\partial \ln c_l^{\pm}}\right)(1-t_+)\nabla(\ln c_l^{\pm})\right]\cdot\nabla\emptyset_l^{\pm}$ | (18) |

Table 2. Summary of boundary conditions in the electrochemical model.

| Physical meaning | Boundary condition | Nº |
|---|---|---|
| Mass conservation | $-D_s^{\pm}\frac{\partial c_s^{\pm}}{\partial r}_{r=0} = 0$ | (19) |
| | $-D_s^{\pm}\frac{\partial c_s^{\pm}}{\partial r}_{r=r_p} = \frac{i_{loc}}{F}$ | (20) |
| | $-D_{l\,eff}^{\pm}\frac{\partial c_l^{\pm}}{\partial z}_{z=L_{neg\,cc}} = -D_{l\,eff}^{\pm}\frac{\partial c_l^{\pm}}{\partial z}_{z=L_{subcell}-L_{pos\,cc}} = 0$ | (21) |
| Charge conservation | $-\sigma_{s\,eff}^{\pm}\cdot\nabla\emptyset_s^{\pm}{}_{z=L_{subcell}-L_{pos\,cc}} = i_{app}$ | (22) |
| | $\emptyset_s^{\pm}{}_{z=L_{neg\,cc}} = 0$ | (23) |
| | $\nabla\emptyset_l^{-}{}_{z=L_{neg\,cc}} = \nabla\emptyset_l^{+}{}_{z=L_{subcell}-L_{pos\,cc}} = 0$ | (24) |

## 2.2 Thermal model applied to a 3D cell domain

The thermal model is applied to the cell domain, which is treated as a homogeneous volume characterized by its effective anisotropic thermophysical properties. The model is based on the following assumptions:

- Heat generation rate and dissipation effects at the battery tabs connection are negligible.
- Thermal radiation from the battery cell surface is negligible.
- The cell effective anisotropic thermophysical properties are deemed not to change within the temperature range considered in this study.

Energy Advances Accepted Manuscript

View Article Online
DOI: 10.1039/D6YA00018E

Open Access Article. Published on 10 June 2026. Downloaded on 6/18/2026 2:09:24 PM.
This article is licensed under a Creative Commons Attribution-NonCommercial 3.0 Unported Licence.

These assumptions are deemed valid for BOL battery cells operating within relatively safe temperature ranges (15-50℃). Furthermore, the adoption of advanced metallurgical tab-welding techniques in commercial EV battery cells justifies neglecting battery tab heating effects, and these tabs are typically integrated using robust mechanisms that provide significant thermal insulation. Crucially, as EV battery packs typically operate at relatively low temperatures, convective heat flux is the dominant mode of heat dissipation, thus rendering radiation effects negligible. Therefore, the governing equation is based on the conservation of energy law and is formulated as:

$$\rho_{eff} c_{peff} \frac{\partial T}{\partial t} = \overline{Q}^{*}_{gen} - \nabla \cdot ( - k_{eff,n} \nabla T) \quad (25)$$

$$- k_{eff,n} \frac{\partial T}{\partial n_S} = h(T_S - T_\infty) \quad (26)$$

In Equation (25), $c_{peff}$ (J/(kgK)) denotes the cell effective specific heat capacity, $\rho_{eff}$ (kg/m$^3$) is the cell effective density, and $k_{eff,n}$ (W/(mK)) represents the cell effective anisotropic thermal conductivities. The volumetric heat generation rate, $\overline{Q}^{*}_{gen}$ (W/m$^3$), is hierarchically transmitted from the electrochemical model. For the boundary condition represented in Equation (26), h (W/(m$^2$K)) is the uniform heat transfer coefficient, $T_S$ (ºC) denotes the cell surface temperature, and $T_\infty$ (ºC) represents the ambient temperature. In the present study, the ambient temperature was set to $T_\infty$=24.5ºC, the initial temperature to $T_{initial}$=24.5ºC, and the air conditions to 50% humidity and atmospheric pressure. The convective heat transfer coefficient (h) was set to 27 W/(m²K), a value derived from an independent air dynamics and heat transfer analysis. This coefficient represents the forced convection environment maintained within the thermal chamber during the experimental validation.

The proposed ECT model was built in COMSOL Multiphysics®, leveraging COMSOL's Lithium-ion Battery and Heat Transfer in Solids interfaces. Mesh independence analyses for the domains considered in this study, as well as specific model features, are provided in the Supplementary Information. This ECT model is novel due to its ability to accurately quantify the spatio-temporal temperature responses in pouch cells with counter-tab configuration operating at various C-rates. This capability is enabled by a derived expression for the plane-projected volumetric heat generation rate. Furthermore, this ECT model can accommodate various cell tab configurations and electrode chemistries. Adapting to different tab configurations requires modifications within the sub-cell and cell domains geometries, while incorporating different electrode chemistries necessitates updating the sub-cell layers properties to correctly estimate voltage responses and volumetric heat generation rates.

Energy Advances Accepted Manuscript

## 3. Pouch cell with counter-tab configuration

View Article Online
DOI: 10.1039/D6YA00018E

Open Access Article. Published on 10 June 2026. Downloaded on 6/18/2026 2:09:24 PM.
This article is licensed under a Creative Commons Attribution-NonCommercial 3.0 Unported Licence.

The cell utilized to demonstrate the ECT model proposed in Section 2 corresponds to a 63-Ah pouch-type lithium-ion battery with a nickel-manganese-cobalt (NMC) cathode, referred to hereafter as the NMC-63Ah pouch cell. A schematic of its internal layered structure is depicted in Fig. 1, on its left-hand side. Key specifications of the NMC-63Ah pouch cell are provided in Table 3. The cell internal structure consists of periodic layer arrangements (sub-cells), composed of a cathode (positive electrode), an anode (negative electrode), a separator, and positive and negative current collectors. These current collectors are made of aluminum (20 μm thick) and copper (10 μm thick), respectively. The NMC-63Ah pouch cell is formed by electrically connecting 84 of these sub-cells in a parallel configuration, with the positive and negative tabs from the current collectors exiting at opposite sides of the cell.

Table 3. Main specifications of the NMC-63Ah pouch cell. Information provided by cell manufacturer.

| Feature | Value |
|---|---|
| Dimensions ($mm^3$) | 256 x 94.5 x 13.8 |
| Total cell area for heat dissipation ($m^2$) | 0.058 |
| Mass (kg) | 0.895 |
| Tab width (mm) | 45 |
| Capacity (Ah) | 63 (at 1/10 C-rate) |
| Minimum voltage (V) | 3.0 |
| Maximum voltage (V) | 4.2 |
| Nominal voltage (V) | 3.7 |
| AC impedance at 1 kHz (mΩ) | 1.5 |
| Cathode chemistry | NMC 811 |
| Anode chemistry | Natural graphite |
| Specific energy density (Wh/kg) | 261 |
| Volumetric energy density (Wh/L) | 644 |
| Cathode material ratio | 97.8% active material<br>1.2% polyvinylidene (PVDF) binder<br>1.0% carbon fibers binder |
| Anode material ratio | 95.6% active material<br>3.4% carboxymethyl cellulose (CMC) binder<br>1.0% Styrene-Butadiene Rubber (SBR) binder |

The parameters used in the electrochemical model for this cell are listed in Table 4. For the separator domain, the parameters correspond to those of the electrolyte, as Li-ion transport occurs exclusively in the liquid phase within this region.

Table 4. Parameters utilized in the electrochemical model for the NMC-63Ah pouch cell.

Energy Advances Accepted Manuscript

View Article Online
DOI: 10.1039/D6YA00018E

Open Access Article. Published on 10 June 2026. Downloaded on 6/18/2026 2:09:24 PM.
This article is licensed under a Creative Commons Attribution-NonCommercial 3.0 Unported Licence.

| Parameter | Cathode | Separator | Anode |
|---|---|---|---|
| Layer thickness (L, μm) | 60[a] | 20[a] | 70[a] |
| Particle radius ($r_p$, μm) | 5[a] | - | 5[a] |
| Solid volume fraction ($\varepsilon_s$) | 0.45[a] | - | 0.50[a] |
| Liquid volume fraction ($\varepsilon_l$) | 0.55[a] | 0.4[a] | 0.50[a] |
| Maximum Li-ion concentration ($c_{s,max}$, mol/m$^3$) | 50,060[b] | - | 31,507[b] |
| Ion migration number ($t_+$) | - | 0.363[c] | - |
| Initial Li-ion concentration ($c_0$, mol/m$^3$) | 1,000[b] | 1,000[b] | 1,000[b] |
| Activation energy for diffusion ($E_{aD}$, J/mol) | 9,978[d] | - | 68,025[d] |
| Diffusion coefficient at reference temperature ($D_{ref}$, m$^2$/s) | $5.0\cdot10^{-13}$ [d] | - | $1.45\cdot10^{-13}$ [d] |
| Electrical/ionic conductivity (σ, S/m) | 0.5[b] | Equation (30)[b] | 100[b] |
| Conversion factor ($a_k$) | 0.5[b] | - | 0.5[b] |
| Transfer coefficient (α) | 0.5[e] | - | 0.5[e] |
| Reaction rate constant (κ, m/s) | $1\cdot10^{-11}$ [e] | - | $1\cdot10^{-11}$ [e] |

[a]: Information provided by cell manufacturer.
[b]: Assumed from [35] for a cell with the same chemistry, similar capacity, form factor, and tab configuration.
[c]: Assumed from [36] for a cell with the same chemistry.
[d]: Assumed from COMSOL Multiphysics material database.
[e]: Assumed from [37] for a cell with the same chemistry.

The temperature-dependent mathematical expressions for the solid phase diffusion coefficient of the positive ($D_S^+$) and negative ($D_S^-$) electrodes, the liquid phase diffusion coefficient ($D_l$), and the electrolyte ionic conductivity ($\sigma_l$) are described as follows:

$$D_s^+ = D_{ref}^+ \exp\left(\frac{E_{aD}^+}{R}\cdot\left(\frac{1}{T_{ref}}-\frac{1}{T}\right)\right) \quad (27)$$

$$D_s^- = D_{ref}^- \exp\left(\frac{E_{aD}^-}{R}\cdot\left(\frac{1}{T_{ref}}-\frac{1}{T}\right)\right) \quad (28)$$

$$D_l = 10^{\left(-8.43-\frac{54}{T-229-0.05c_l}-2.2\cdot10^{-4}c_l\right)} \quad (29)$$

$$\sigma_l = 1\cdot10^{-4}\cdot \left(-8.2488+0.053248T-2.9871\cdot10^{-5}T^2+0.2623\cdot10^{-3}c_l-9.3063\cdot10^{-6}c_lT+8.069\cdot10^{-9}c_lT^2+0.22002\cdot10^{-6}c_l^2\right. \quad (30)$$

Where $c_l$ (mol/m$^3$) is the Li-ion concentration, F represents the Faraday constant (96,485 C/mol), η (V) quantifies the electrode overpotential, R represents the gas constant (8.314 J/(molK)), $T_{ref}$ (298 K) is the referential temperature, and T (K) is the temperature.

Energy Advances Accepted Manuscript

View Article Online
DOI: 10.1039/D6YA00018E

Open Access Article. Published on 10 June 2026. Downloaded on 6/18/2026 2:09:24 PM.
This article is licensed under a Creative Commons Attribution-NonCommercial 3.0 Unported Licence.

This ECT model is used to simulate constant current (CC) discharge processes over the 80%-20% state-of-charge (SOC) window, and three distinct current profiles were applied to the NMC-63Ah pouch cell: 1C-rate (63 A), 1.5C-rate (94.5 A), and 2C-rate (126 A). Discharge profiles were prioritized because of their more aggressive operational conditions: the cell manufacturer specifies a maximum 2C-rate for discharge, compared to a maximum 1C-rate for charge. Evaluating high C-rates enables a critical assessment of maximum temperature and hot spots. The 80%-20% SOC window ensures the exclusion of extreme SOC conditions as per the cell manufacturer guidelines. For the thermal model, the cell effective anisotropic thermophysical properties were obtained from a multi-length-scale analysis as per our prior work [13], and their values are $k_{eff\ in\text{-}plane}$= 27.5 W/(mK) (xx-yy direction in Fig. 1), $k_{eff\ cross\text{-}plane}$= 0.29 W/(mK) (zz direction in Fig. 1), and $c_{peff}$= 1,207 J/(kgK). A comparison of the experimentally measured voltage responses and transient temperatures with numerical predictions is presented in Section 5, which enables the identification of localized hot spots. Furthermore, these findings serve as a reliable basis for assessing the cell thermal behavior under different demanding conditions, including representative dynamic driving profiles [38].

## 4. Experimental setup and data acquisition

To validate the proposed ECT model, the current profiles described in the previous section were experimentally applied to the NMC-63Ah pouch cell. During testing, the cell was placed within a thermal chamber with controlled environmental conditions, and the tabs were connected to power cables to apply the current profiles. Thermocouples and voltage sensors recorded temperature and voltage transient responses, which were then compared to the numerical predictions. A brief overview of the key equipment used in the experimental setup is provided below:

(i) Thermal chamber

The thermal chamber used in this study provides controlled ambient temperature ($T_\infty$). The specific model, Espec EPX-4HF, is shown in Fig. 2(a). With an internal volume of 1,000 L, this chamber offers a temperature range from -70ºC to 124ºC and maintains a fluctuation below ± 0.5ºC, ensuring safe and reliable conditions. The chamber is equipped with top-mounted blowers capable of 800 $ft^3$/min airflow, enabling the maintenance of $T_\infty$=24.5ºC. Positioning the cell at the center of the chamber ensures nearly uniform convective conditions on both cell surfaces – an experimentally confirmed assumption that is later employed in the numerical simulations.

(ii) Battery cell cycler

A battery cell cycler, model Chroma 17010, was utilized to apply the different current profiles to the NMC-63Ah pouch cell, enabling measurement of transient voltage and temperature responses. The cycler features 24

Energy Advances Accepted Manuscript

View Article Online
DOI: 10.1039/D6YA00018E

independent channels, each capable of delivering 0-6 V and up to 100 A. For tests requiring higher current levels, three channels were connected in parallel, allowing a current output to meet the experimental power requirements.

(iii) Temperature sensors

Thirteen T-type thermocouples (accuracy ± 0.5ºC) were employed to measure the cell surface and ambient temperature. As shown in Fig. 2(b), 12 thermocouples were attached to the cell surfaces – six on each side – while one was placed to monitor the ambient temperature. For each test case, the cell was divided into six representative regions to capture the expected temperature gradients resulting from current concentration effects near the tabs. To ensure spatial correspondence, thermocouples T1-T6 were installed on one side, with T7-T12 placed directly opposite T1-T6, respectively, allowing symmetric thermal mapping across the cell surfaces.

(iv) Battery holder

To replicate the cell operational orientation within a real EV battery pack, a custom-made cell holder was designed and fabricated. The structure combines 80/20 aluminum framing with 3D-printed Polyethylene Terephthalate Glycol (PETG) components that support the cell along its laminated edges, ensuring vertical alignment, mechanical stability, and full exposure of the cell surfaces to the convective environment for uniform thermal conditions.

(v) Clamp connections

Electrical connections and voltage measurements were established using clamps in direct contact with the cell tabs. The power cables were secured to the clamps using standard nuts.

Open Access Article. Published on 10 June 2026. Downloaded on 6/18/2026 2:09:24 PM.
This article is licensed under a Creative Commons Attribution-NonCommercial 3.0 Unported Licence.

Energy Advances Accepted Manuscript

View Article Online
DOI: 10.1039/D6YA00018E

Open Access Article. Published on 10 June 2026. Downloaded on 6/18/2026 2:09:24 PM.
This article is licensed under a Creative Commons Attribution-NonCommercial 3.0 Unported Licence.

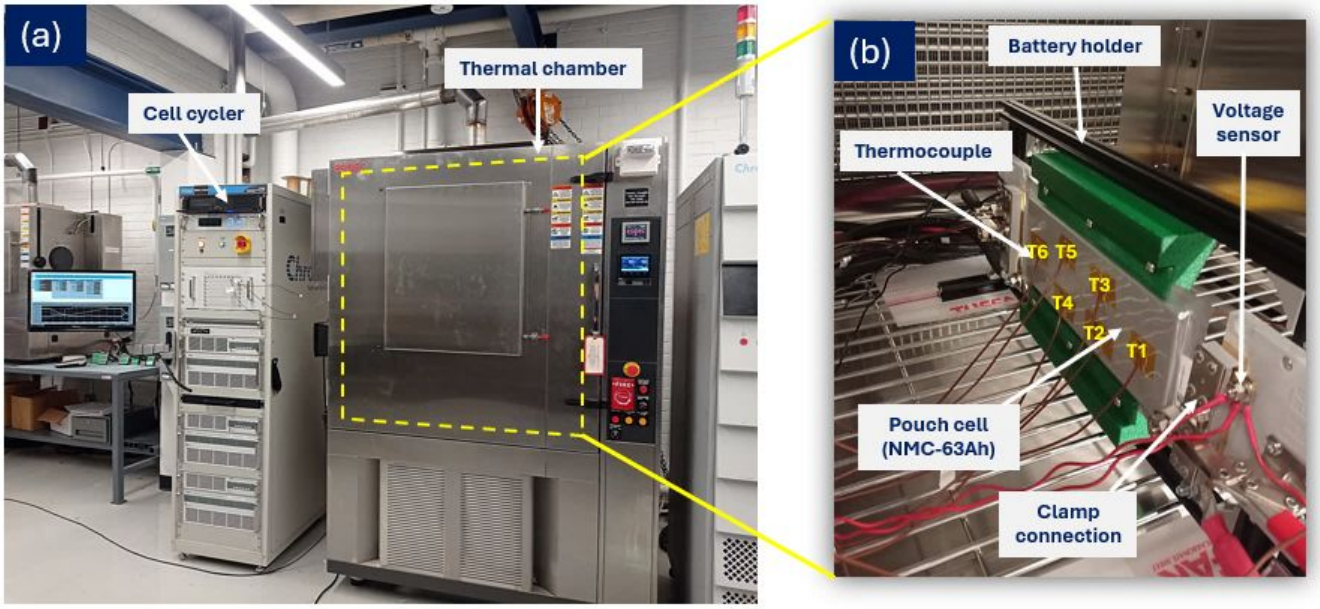


Fig. 2. Experimental setup for NMC-63Ah pouch cell testing. (a) Primary equipment, including cell cycler for current profile implementation and thermal chamber for environmental control. (b) Detailed view of vertically oriented NMC-63Ah pouch cell, illustrating placement of thermocouples on the cell surface, along with voltage sensor lead and clamp connections in battery holder.

## 5. Validation of the ECT model

Experimental validation of the proposed ECT model is presented in Figs. 3 and 4, which compare experimental measurements and numerical simulations for voltage responses and cell surface temperatures, respectively. To ensure repeatability of the experimental temperatures, the measurements were taken across three distinct cell samples, and error bars were included in Fig. 4 around averages. In addition, a Root Mean Square Deviation ($RMSD_T$) approach was implemented for the temperatures comparison to comprehensively quantify the predictive accuracy of the proposed ECT model, as defined by Equation (31) below.

$$RMSD_T = \sqrt{\frac{\sum_{t=0}^{T} \sum_{i=1}^{N} \left(T_{i,t,\,exp} - T_{i,t,\,num}\right)^2}{N}} \quad (31)$$

Where N is the number of measurements (six thermocouples, every three seconds), $T_{i,t,exp}$ is the measured value for the thermocouple #i at the time t, and $T_{i,t,num}$ corresponds to the simulated value for the thermocouple #i at the time t.

Figure 3 compares the experimental voltage responses with numerical simulations from the ECT model for the C-rates considered in this study. This comparison confirms the model's high accuracy, as the numerical simulations closely match the experimental measurements. The maximum difference is 0.082V (2.1%) for the 2C-



Energy Advances Accepted Manuscript

View Article Online
DOI: 10.1039/D6YA00018E

Open Access Article. Published on 10 June 2026. Downloaded on 6/18/2026 2:09:24 PM.
This article is licensed under a Creative Commons Attribution-NonCommercial 3.0 Unported Licence.

rate scenario, occurring at the beginning of the discharge process. This may be attributed to two main factors: the deceleration of Li-ions mobility at lower temperatures [39], and the high polarization caused by an aggressive C-rate at the beginning and the end of discharge [36]. The maximum difference between experimental voltage responses and numerical simulations decreases with less aggressive C-rates: 0.075V (1.9%) for 1.5C-rate, and 0.064V (1.6%) for 1C-rate. This level of accuracy in predicting voltage responses aligns well with other electrochemical-thermal models in literature, such as those from He et al.[24], Lin et al.[25], and Samba et al.[26], demonstrating that the proposed ECT model accurately predicts the cell electrochemical performance. This voltage prediction is essential because the magnitude and spatial distribution of the volumetric heat generation rate depend strongly on it, and it enables further analysis, such as optimizing electrode layouts.

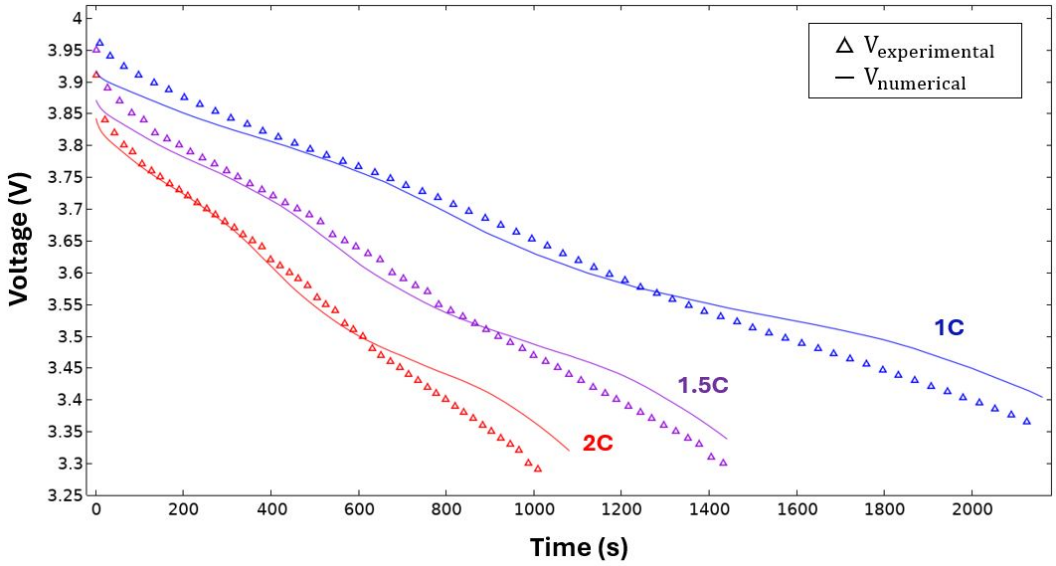


Fig. 3. Experimental measurements of voltage responses (Δ) and numerical simulations from ECT model (-) during CC discharge profiles of 1C, 1.5C, and 2C-rate applied to NMC-63Ah pouch cell across 80%-20% SOC window.

Figure 4 compares the experimental measurements of the cell surface temperatures with numerical simulations at 1C, 1.5C, and 2C rates of CC discharge. The analysis is focused on thermocouples T1 and T5, as these locations exhibit the maximum measured temperature gradients across the cells. While the experimental data were recorded every three seconds, the figure displays a subset of points to maintain visual clarity (13 points for 1C-rate, 14 points for 1.5C-rate, and 13 points for 2C-rate). The ECT model simulations show strong agreement with the measured values, remaining within the experimental error bars for most of the discharge period across all C-rates. Quantification of discrepancies via $RMSD_T$ – calculated considering six thermocouples – yielded values of 0.404ºC, 0.528ºC, and 0.714ºC for the 1C, 1.5C, and 2C-rate scenarios, respectively. The increase in the $RMSD_T$ at

Energy Advances Accepted Manuscript

View Article Online
DOI: 10.1039/D6YA00018E

Open Access Article. Published on 10 June 2026. Downloaded on 6/18/2026 2:09:24 PM.
This article is licensed under a Creative Commons Attribution-NonCommercial 3.0 Unported Licence.

higher C-rates suggests that temperature prediction becomes more difficult under aggressive current profiles due to elevated volumetric heat generation rate driven by the voltage estimations. However, these discrepancies remain within acceptable limits. The maximum measured temperature at each C-rate was consistently recorded by thermocouple T1, near the positive tab, indicating localized volumetric heat generation rate driven by the concentration of current density in this region. As expected, temperature rise scales with the C-rate: the 1C-rate case exhibits an average increase of 0.15ºC/min, while this metric is 0.77ºC/min for the 2C-rate scenario, 5.13 times higher for the double current profile and the same environmental convective conditions. Higher C-rates induced increasing spatial temperature gradients in the cell surface, which doubled from 0.9ºC (1C-rate) to 1.8ºC (2C-rate) by the end of discharge, highlighting that the NMC-63Ah pouch cell reaches non-uniform temperature fields at different current profiles for a given uniform convective environment. Overall, this validated ECT model accurately quantifies spatial temperature fields, identifying localized hot spots that contribute to non-uniform degradation and lifespan reduction. As industry trends shift toward higher C-rate capabilities, precise predictions of spatio-temporal temperatures in pouch cells are paramount, given the expected increases in maximum cell temperature and spatial temperature gradients. In particular, the development of fast-charging and high-power-discharge technologies must account for the aggressive thermal conditions experienced by large-format pouch cells.

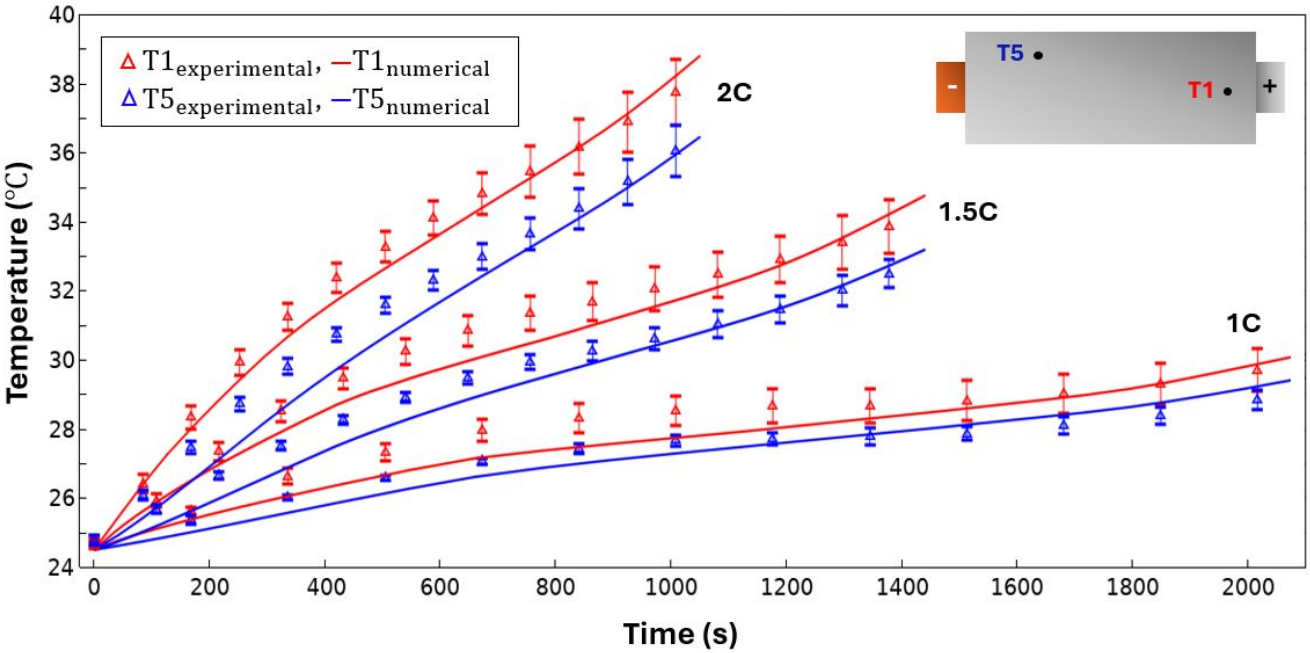


Fig. 4. Transient temperature measurements (Δ) and numerical simulations from ECT model (-) for thermocouples T1 and T5 during CC discharge profiles of 1C, 1.5C, and 2C-rate applied to NMC-63Ah pouch cell across 80%-20% SOC window. Experimental measurements represent the average of three different cells with standard deviation shown as error bars.

Energy Advances Accepted Manuscript

View Article Online
DOI: 10.1039/D6YA00018E

Open Access Article. Published on 10 June 2026. Downloaded on 6/18/2026 2:09:24 PM.
This article is licensed under a Creative Commons Attribution-NonCommercial 3.0 Unported Licence.

Figure 5 illustrates three-dimensional (3D) contours of volumetric heat generation rates ($Q_{gen}$, in kW/m$^3$) and temperature fields (T, in ºC) obtained from the ECT model at the end of discharge (SOC 20%) for 1C-rate, 1.5C-rate, and 2C-rate. As is presented in Figs. 5(a) to (c), the volumetric heat generation rate predominantly concentrates near the cell tabs. Specifically, the region adjacent to the positive tab exhibits the maximum $Q_{gen}$ across the tests, which is consistent with the higher temperature measurements of thermocouple T1 (Fig. 4). The localized volumetric heat generation rate is driven by the current density concentration. At the 1C-rate scenario, the highest current density near the positive tab is 1.57 MA/m$^2$, causing a maximum $Q_{gen}$ of 70 kW/m$^3$, whereas the highest current density in this region is 3.14 MA/m$^2$ for the 2C-rate, yielding a maximum $Q_{gen}$ of 280 kW/m$^3$, results that are aligned with the quadratic relation between current profile and magnitude of volumetric heat generation rate. In addition to the $Q_{gen}$ intensity, the level of non-uniformity is also exacerbated with higher C-rates. For instance, the maximum $Q_{gen}$ of 70 kW/m$^3$ for the 1C-rate case corresponds to 3.9 times the average (18 kW/m$^3$), whereas the maximum $Q_{gen}$ of 280 kW/m$^3$ in the 2C-rate case is 4.5 times the average (62 kW/m$^3$). The non-uniformity of $Q_{gen}$ triggers non-uniform temperature fields throughout the cell domain. As Fig. 5(d) presents for the 1C-rate scenario, the maximum temperature ($T_{max}$) remains within the safety limits with a value of 31.3ºC, having spatial uniformity with a maximum spatial temperature gradient ($\Delta T_{max}$) of 1.7ºC. On the other hand, the optimal thermal conditions are exceeded at the 2C-rate case. Whereas $T_{max}$ reaches 42.4ºC, $\Delta T_{max}$ is 5.9ºC, conditions that are detrimental to cell safety and reliability, as these levels for $T_{max}$ and $\Delta T_{max}$ are known to accelerate non-uniform cell degradation. These 3D analyses of $Q_{gen}$ and temperature fields in the NMC-63Ah pouch cell highlight the necessity of (i) reduction of current density from the cell layers layout – a topic that is analyzed in the next section – and (ii) BTMS strategies aimed at localized heat dissipation. Further investigation of (i) and (ii) can be directly guided by this ECT model thanks to its ability to predict spatio-temporal temperature fields and localized hot spots, enabling extensions of thermal modeling studies to module and pack levels where the through-thickness thermal gradients become more relevant due to the inter-cell materials, such as foam layers and metal fins. Furthermore, the anticipated progression toward higher C-rate capabilities driven by fast-charging/discharging requirements will impose more severe thermal stress on pouch cells, underscoring the need for further investigation into the above-mentioned topics (i) and (ii).

Energy Advances Accepted Manuscript

View Article Online
DOI: 10.1039/D6YA00018E

Open Access Article. Published on 10 June 2026. Downloaded on 6/18/2026 2:09:24 PM.
This article is licensed under a Creative Commons Attribution-NonCommercial 3.0 Unported Licence.

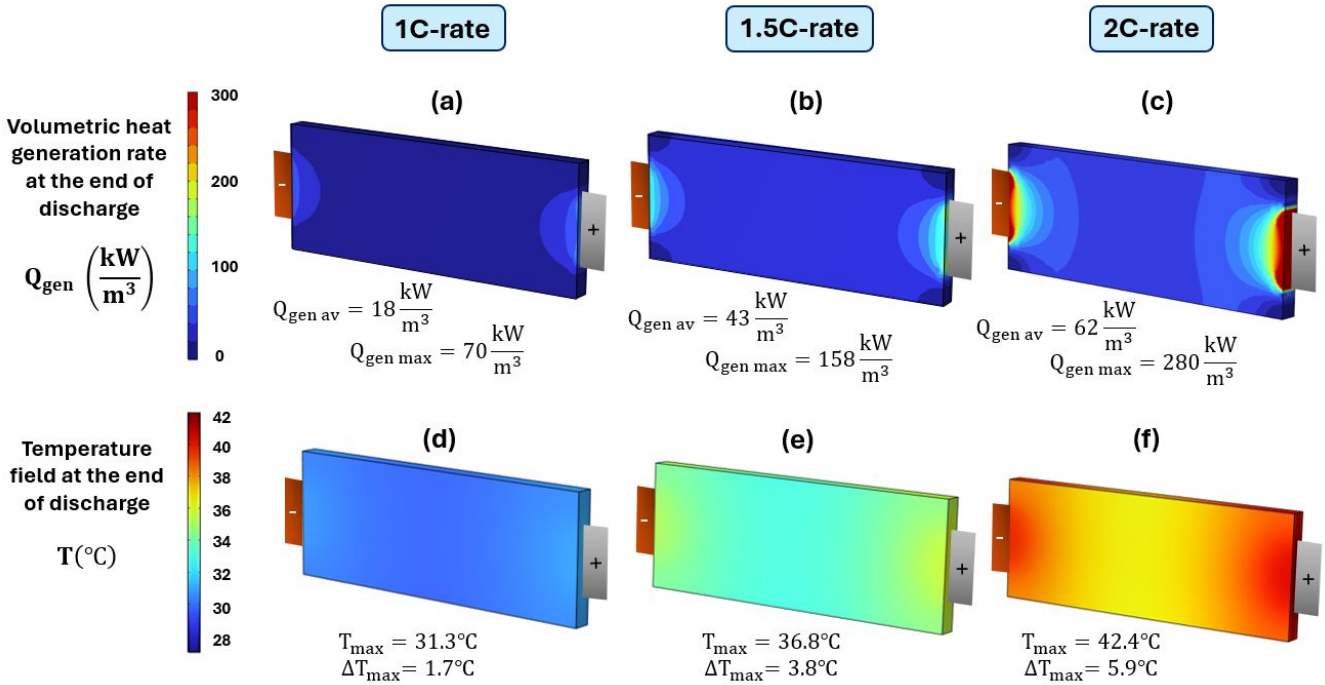


Fig. 5. Three-dimensional volumetric heat generation rates ($Q_{gen}$) and temperature fields at end of discharge (SOC 20%) for NMC-63Ah pouch cell under different CC discharge profiles. Contours of $Q_{gen}$ are presented in (a) 1C-rate, (b) 1.5C-rate, and (c) 2C-rate, detailing average ($Q_{gen\ av}$) and maximum values ($Q_{gen\ max}$). Temperature fields are illustrated in (d) 1C-rate, (e) 1.5C-rate, and (f) 2C-rate, indicating maximum temperature ($T_{max}$) and maximum spatial temperature gradient ($\Delta T_{max}$).

## 6. Sensitivity of Cell Thermal Performance to Select Electrode Parameters and Cell Tabs

To assess how modifications at the sub-cell layers affect the overall cell thermal performance, this section presents a sensitivity analysis focused on the electrode layers and cell tabs. The electrode parameters listed in Table 4 and tab width presented in Table 3 are taken as the baseline, with variations applied one at a time to isolate their individual effects. The parameters selected for variation include electrode thickness and solid volume fraction due to their influence on volumetric heat generation rate magnitude (Equations (15)-(18) in Table 1), and cell tab width as per their impact on the current density concentration. The effects of electrode particle radius (which affects the effective specific surface area in the numerical model) are discussed in the Supplementary Information (Fig. A2). This sensitivity analysis assumes the same environmental convective conditions from the experimental setup (h = 27 W/(m$^2$K) and $T_\infty$ = 24.5 ºC), and evaluates the cell volumetric heat generation rate ($Q_{gen}$), maximum temperature ($T_{max}$), and maximum spatial temperature gradient ($\Delta T_{max}$) during a profile of CC discharge at 2C-rate (the most aggressive current) across the SOC 80%-20% window. Also, although their variations are relatively small, the cell effective thermophysical properties were updated with the electrode thickness and solid volume fraction, as

Energy Advances Accepted Manuscript

View Article Online
DOI: 10.1039/D6YA00018E

Open Access Article. Published on 10 June 2026. Downloaded on 6/18/2026 2:09:24 PM.
This article is licensed under a Creative Commons Attribution-NonCommercial 3.0 Unported Licence.

presented in our previous article [13]. The specific parameter values used in this sensitivity analysis are provided in Table 5:

Table 5. Selected parameters for the sensitivity analysis. The lower and upper electrode values around the baseline scenario (Table 4) cover typical ranges for these parameters reported in the literature [40,41].

| Parameter | Values for evaluation |
|---|---|
| Cathode thickness, $L_{pos}$ (μm) | 35, 60[a], 80 |
| Anode thickness, $L_{neg}$ (μm) | 42, 70[a], 102 |
| Cathode solid volume fraction, $\varepsilon_s^+$ | 0.35, 0.45[a], 0.75 |
| Anode solid volume fraction, $\varepsilon_s^-$ | 0.40, 0.50[a], 0.68 |
| Cell tab width (mm) | 30, 45[a], 70 |

[a]: Baseline value

### 6.1 Effect of Electrode Thickness

Figure 6 presents how variations in the thickness of cathode ($L_{pos}$) and anode ($L_{neg}$) layers impact on the volumetric heat generation rate, $Q_{gen}$, and thermal response, $T_{max}$ and $\Delta T_{max}$. The results indicate that $Q_{gen}$ is more sensitive to the cathode layer thickness ($L_{pos}$, in Fig. 6(a-1)) than the anode layer thickness ($L_{neg}$, in Fig. 6(b-1)) during the discharge process. This finding aligns with our previous work of thermal transport across multiple length scales in EVs [13]. The main reason for this behavior is as follows: while increasing the cathode thickness directly increases the cell capacity, it concurrently affects two factors that elevate the volumetric heat generation rate. First, it extends the Li-ion propagation path during discharge, which increases the cell internal resistance. Second, a thicker cathode layer means that more available Li-ions come from the anode in a discharge process, which further contributes to elevated volumetric heat generation rate. In turn, this greater volumetric heat generation rate drives higher values for both $T_{max}$ and $\Delta T_{max}$. This effect is demonstrated in Figs. 6(a-2) and 6(a-3), where a cathode layer thickness of 80 μm results in thermal conditions that are detrimental to cell lifespan, performance, and safety. From a thermal-design perspective, these results indicate that thinner cathode layers are thermally preferable when targeting a fixed capacity, as they mitigate excessive volumetric heat generation rate and temperature non-uniformity.

Energy Advances Accepted Manuscript

View Article Online
DOI: 10.1039/D6YA00018E

Open Access Article. Published on 10 June 2026. Downloaded on 6/18/2026 2:09:24 PM.
This article is licensed under a Creative Commons Attribution-NonCommercial 3.0 Unported Licence.

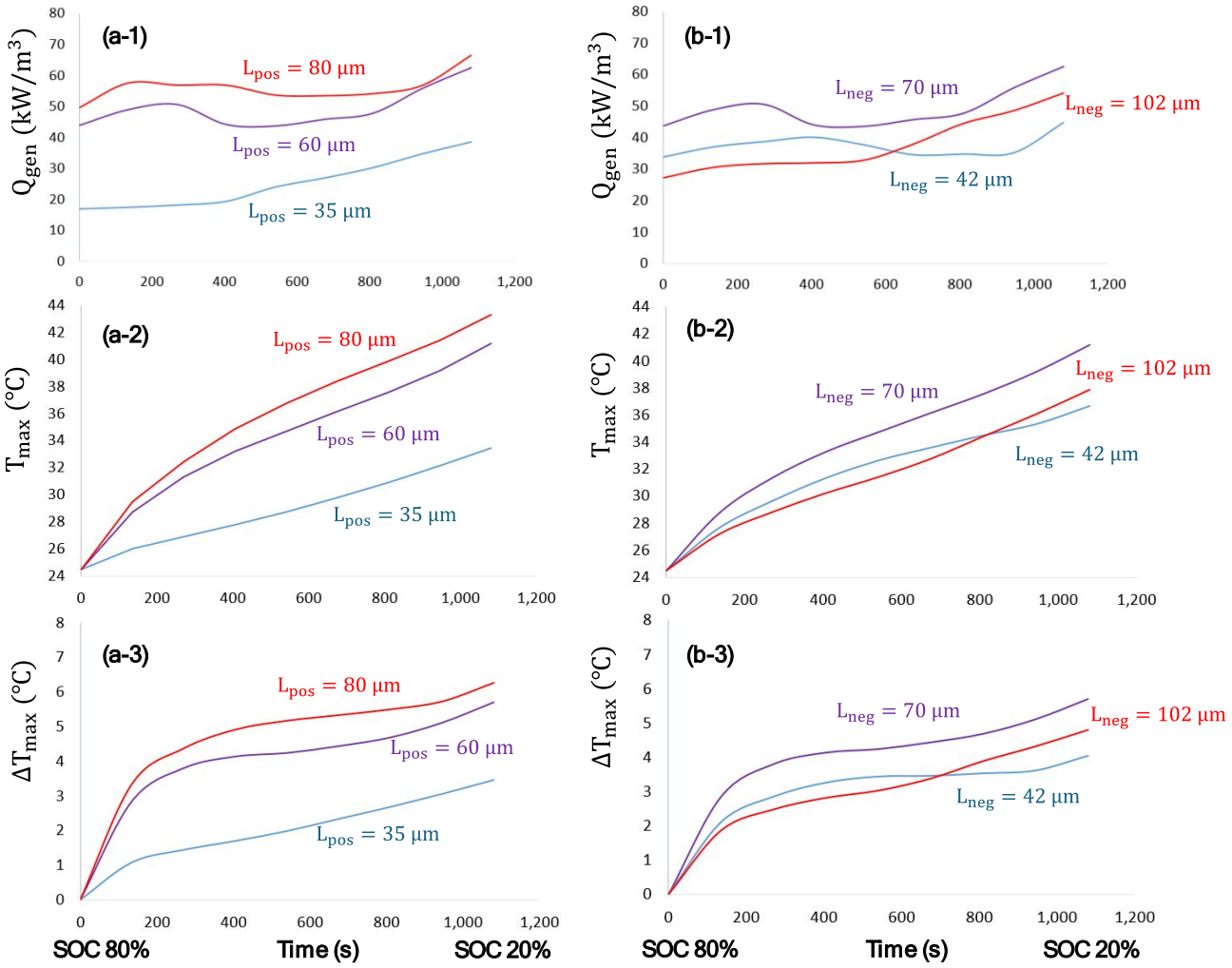


Fig. 6. Sensitivity analysis of cell thermal performance with respect to changes in electrode thicknesses, showing their impact on cell volumetric heat generation rate ($Q_{gen}$), maximum temperature ($T_{max}$), and maximum spatial temperature gradient ($\Delta T_{max}$). Effects of variations in positive electrode thickness ($L_{pos}$) are presented in (a-1) $Q_{gen}$; (a-2) $T_{max}$; and (a-3) $\Delta T_{max}$, and in negative electrode thickness ($L_{neg}$) are presented in (b-1) $Q_{gen}$; (b-2) $T_{max}$; and (b-3) $\Delta T_{max}$.

### 6.2 Effect of Electrode Solid Volume Fraction

Figure 7 illustrates the impact of variations in the solid volume fraction of the positive electrode ($\varepsilon_s^+$) and the negative electrode ($\varepsilon_s^-$) on $Q_{gen}$, $T_{max}$ and $\Delta T_{max}$. As shown in Figs. 7(a-1) and 7(b-1), the volumetric heat generation rate ($Q_{gen}$) exhibits a higher sensitivity to $\varepsilon_s^+$ than $\varepsilon_s^-$, again consistent with our previous multi-length-scale study [13]. The main reason behind this finding is that higher values of $\varepsilon_s^+$ correspond to a reduced volume of the electrolyte liquid phase within the positive electrode. During discharge, this restricted liquid phase accelerates the accumulation and concentration of Li-ions within the cathode domain – often termed the saturation effect – thereby increasing the internal resistance and the resulting elevated $Q_{gen}$. This greater volumetric heat generation



Energy Advances Accepted Manuscript

View Article Online
DOI: 10.1039/D6YA00018E

Open Access Article. Published on 10 June 2026. Downloaded on 6/18/2026 2:09:24 PM.
This article is licensed under a Creative Commons Attribution-NonCommercial 3.0 Unported Licence.

rate drives higher values for both $T_{max}$ and $\Delta T_{max}$, as detailed in Figs. 7(a-2) and 7(a-3). Given that elevated values of $T_{max}$ and $\Delta T_{max}$ – such as those observed when $\varepsilon_s^+ = 0.75$ – accelerate degradation in LIB cells, optimizing $\varepsilon_s^+$ is essential for maximizing battery lifespan, while acknowledging their influence in the regulation of charge conservation, ionic conductivity and Li-ions transport kinetics.

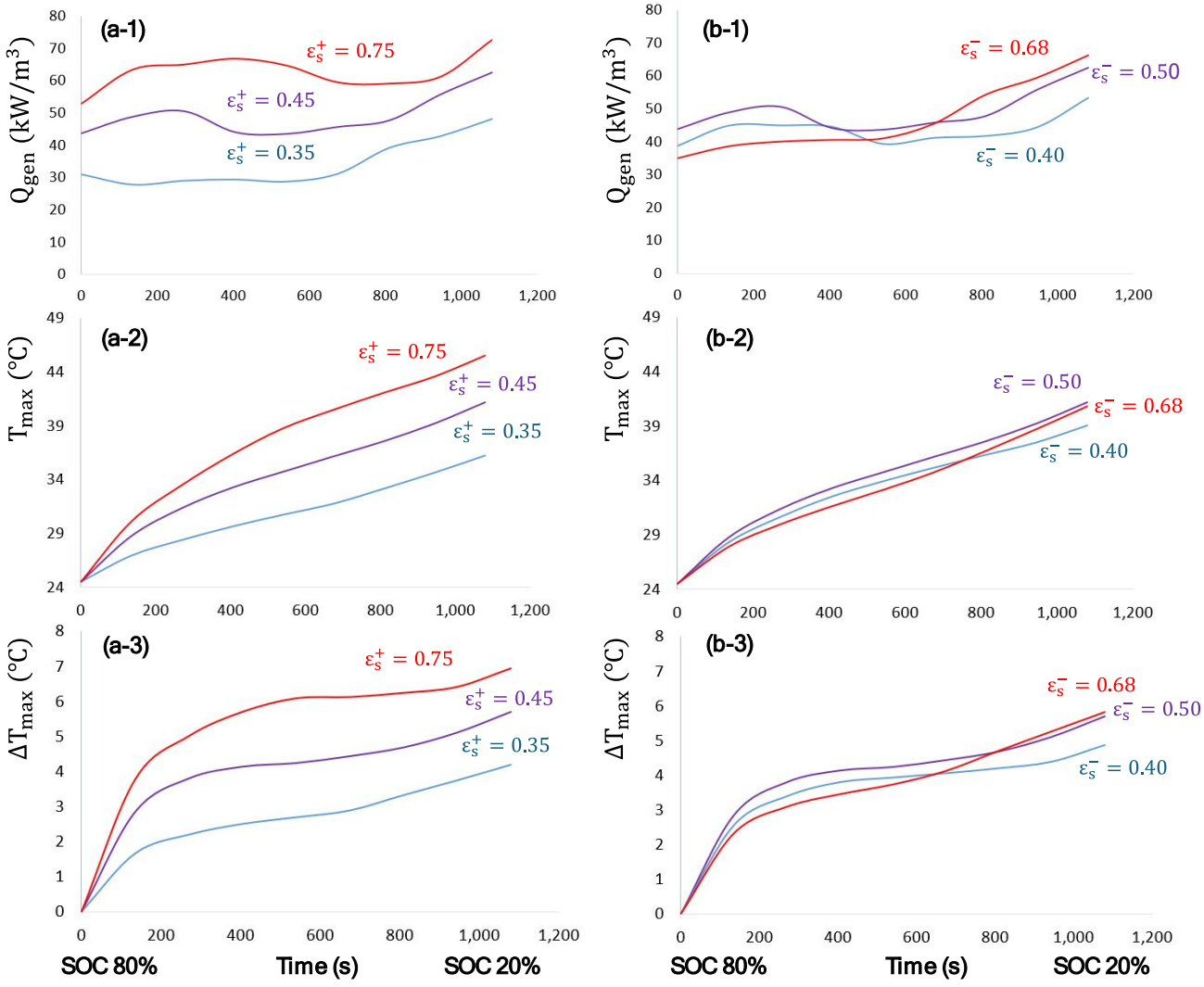


Fig. 7. Sensitivity analysis of cell thermal performance with respect to changes in electrode solid volume fraction, examining their impact on cell volumetric heat generation rate ($Q_{gen}$), maximum temperature ($T_{max}$), and maximum spatial temperature gradient ($\Delta T_{max}$). Effects of variations in positive electrode solid volume fraction ($\varepsilon_s^+$) are presented in (a-1) $Q_{gen}$; (a-2) $T_{max}$; and (a-3) $\Delta T_{max}$, and in negative electrode solid volume fraction ($\varepsilon_s^-$) are presented in (b-1) $Q_{gen}$; (b-2) $T_{max}$; and (b-3) $\Delta T_{max}$.

Energy Advances Accepted Manuscript

View Article Online
DOI: 10.1039/D6YA00018E

Open Access Article. Published on 10 June 2026. Downloaded on 6/18/2026 2:09:24 PM.
This article is licensed under a Creative Commons Attribution-NonCommercial 3.0 Unported Licence.

### 6.3 Effect of Tabs Geometry

Figure 8 demonstrates the strong influence of tab width on the spatial distribution of volumetric heat generation rate by illustrating 3D contours of $Q_{gen}$ and temperature field at the end of discharge (SOC 20%), and demonstrating how these variables respond to changes in the cell tab width. While electrode thickness and solid volume fraction impact the magnitude of volumetric heat generation rate, tab width influences its non-uniformity, current-density localization and the formation of hot spots. For the baseline case (45 mm tab width and 3.14 MA/m$^2$ of maximum current density), the results of $Q_{gen}$ and temperature field are presented Figs. 8(b) and 8(e), respectively. Increasing the tab width to 70 mm reduces the maximum concentration of current density to 2.02 MA/m$^2$, decreasing the maximum $Q_{gen}$ to 115 kW/m$^3$ (Fig. 8(a)), thus lowering $T_{max}$ and $\Delta T_{max}$ to safer levels (Fig. 8(d)). Conversely, narrowing the tabs to 30 mm intensifies localized volumetric heat generation rate to 630 kW/m$^3$ (Fig. 8(c)) due to an increased maximum current density of 4.71 MA/m$^2$, resulting in more pronounced hot spots near the tabs (Fig. 8(f)) – a condition that compromises cell safety, reliability, and degradation uniformity. This analysis reveals that the dimensions of the cell tabs significantly impact the spatial distribution of the volumetric heat generation rate (without affecting the average magnitude), in turn causing different temperature fields and localized hot spots for a given current profile and heat-dissipation condition.

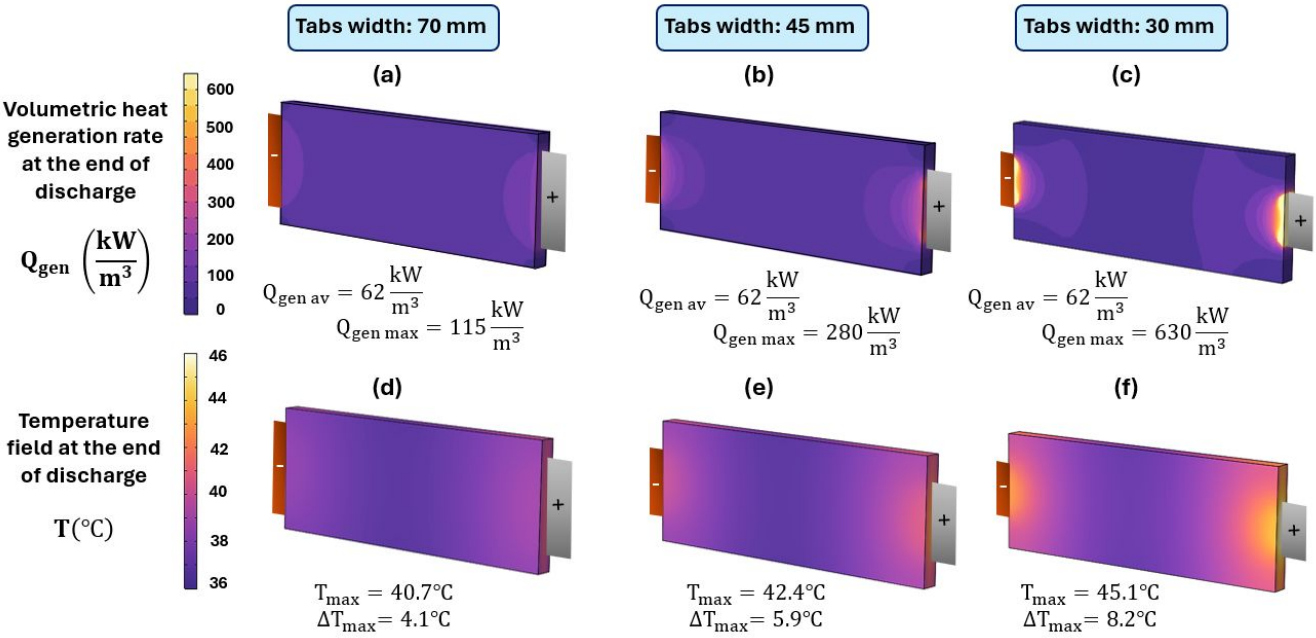


Fig. 8. Sensitivity analysis of cell thermal performance with variations in tab width at end of discharge (SOC20%). Contours of volumetric heat generation rate ($Q_{gen}$) are shown for tab width of (a) 70 mm; (b) 45 mm, and (c) 30 mm, detailing average ($Q_{gen\,av}$) and maximum ($Q_{gen\,max}$) values. The corresponding temperature fields, including $T_{max}$ and $\Delta T_{max}$, are presented for tab width of (d) 70 mm; (e) 45 mm, and (f) 30 mm.

Energy Advances Accepted Manuscript

View Article Online
DOI: 10.1039/D6YA00018E

Open Access Article. Published on 10 June 2026. Downloaded on 6/18/2026 2:09:24 PM.
This article is licensed under a Creative Commons Attribution-NonCommercial 3.0 Unported Licence.

These results clearly demonstrate that cell tab geometry is an important design parameter for controlling spatial thermal behavior in large-format pouch cells, particularly for counter-tab configuration.

## 7. Conclusions

In this study, we developed a three-dimensional (3D) electrochemical-thermal (ECT) coupled model for lithium-ion pouch cells with counter-tab configuration, specifically designed to achieve high-fidelity spatio-temporal temperature predictions. This model employs a hierarchical domain structure, linking sub-cell-level electrochemical processes with anisotropic cell-level thermal transport through a bi-directional exchange framework of volumetric heat generation rate and temperature field. A key novelty of this work is the introduction of a heat-generation distribution factor that accurately captures non-uniform Joule heat generation influenced by the current density concentration in the metal current collectors near the cell tabs, thereby overcoming the limitations of conventional plane-averaged projection methods. By numerically solving the governing electrochemical and energy equations, this ECT model accurately quantifies transient phenomena, including voltage responses, spatially distributed volumetric heat generation rate, and spatio-temporal temperatures.

The ECT coupled model offers essential insights for advancing pouch cell design. After being experimentally validated at different discharge C-rates, this model was used to perform a sensitivity analysis assessing the influence of electrode design parameters (thickness and solid volume fraction) and cell tab geometry on cell volumetric heat generation rate, maximum temperature, and maximum spatial temperature gradient. Results showed that the cathode design parameters affect the overall volumetric heat generation rate, while tab geometry governs its spatial distribution and the formation of localized hot spots. Thinner electrodes and lower cathode solid volume fractions are thermally beneficial, while wider tabs significantly reduce the concentration of current density, in turn decreasing localized volumetric heat generation rate and spatial temperature gradients.

By accurately identifying localized hot spots and their underlying causes, the proposed ECT model provides a powerful tool for guiding electrode design and strategies for localized heat dissipation. Overall, this work contributes to understanding and managing these complex thermal gradients in large-format pouch cells, supporting the development of more efficient, durable, and higher-performance battery systems for EV applications.

Energy Advances Accepted Manuscript

View Article Online
DOI: 10.1039/D6YA00018E

Open Access Article. Published on 10 June 2026. Downloaded on 6/18/2026 2:09:24 PM.
This article is licensed under a Creative Commons Attribution-NonCommercial 3.0 Unported Licence.

Energy Advances Accepted Manuscript

## Author contributions

The manuscript was written with contributions from all authors. All authors have approved the final version of the manuscript. **Oscar A. Alvarez**: conceptualization, methodology, data acquisition, formal analysis, and original manuscript writing. **Carlos M. Da Silva**: project administration, supervision, funding acquisition, visualization, review & editing. **Cristina H. Amon**: conceptualization, formal analysis, funding acquisition, supervision, visualization, review & editing.

## Data availability statement

Data will be made available on request.

## Conflicts of interest

There are no conflicts to declare.

## Acknowledgement

The authors gratefully acknowledge the Natural Sciences and Engineering Research Council of Canada (NSERC), the Ontario Research Fund – Research Excellence (ORF-RE) program, Flex-N-Gate, and Mitacs for their financial support, as well as CMC Microsystems for providing the CAD tools that facilitated this research.

## Nomenclature

| | | | |
|---|---|---|---|
| A | Area ($m^2$) | t | Time (s) |
| $c_p$ | Specific heat capacity ($J/(kgK)$) | $t_+$ | Lithium-ion transfer number |
| c | Lithium-ion concentration ($mol/m^3$) | V | Voltage (V) |
| D | Diffusion coefficient ($m^2/s$) | α | Transfer coefficient |
| $\varepsilon_l$ | Liquid volume fraction | $\varepsilon_s$ | Solid volume fraction |
| E | Potential (V) | η | Local over potential (V) |
| F | Faraday constant (96,485 C/mol) | k | Thermal conductivity ($W/(mK)$) |
| h | Heat transfer coefficient ($W/(m^2K)$) | ρ | Density ($kg/m^3$) |
| i | Current density ($A/m^2$) | σ | Ionic/electric conductivity ($S/m$) |
| κ | Reaction rate constant ($m^{2.5}/(mol^{0.5}s)$) | $S_a$ | Specific surface area ($1/m$) |
| L | Thickness (μm) | γ | Bruggeman exponent |
| T | Temperature (°C) | ϕ | Phase potential (V) |
| R | Gas constant ($8.314\ J/(mol\ K)$) | $r_p$ | Particle radius of electrodes (μm) |
| $Q_{gen}$ | Volumetric heat generation rate ($W/m^3$) | df | Distribution factor |

View Article Online
DOI: 10.1039/D6YA00018E

Open Access Article. Published on 10 June 2026. Downloaded on 6/18/2026 2:09:24 PM.
This article is licensed under a Creative Commons Attribution-NonCommercial 3.0 Unported Licence.

## Acronyms

| | | | |
|---|---|---|---|
| Lithium-ion battery | LIB | Battery Thermal Management System | BTMS |
| Electric vehicle | EV | Battery Energy Storage System | BESS |
| Root Mean Square Deviation | $RMSD_T$ | Electrochemical-thermal | ECT |
| State-of-Charge | SOC | Beginning-of-life | BOL |
| Pseudo-Two-Dimensional | P2D | Nickel-Manganese-Cobalt | NMC |
| Equivalent-Circuit-Model | ECM | Lithium-ion | Li-ion |

## References

1. Rana S, Kumar R, Bharj RS. Lithium-Ion Battery Thermal Management Techniques and Their Current Readiness Level. *Energy Technol*. Published online January 1, 2022. doi:10.1002/ente.202200873

2. Shen ZG, Chen S, Liu X, Chen B. A review on thermal management performance enhancement of phase change materials for vehicle lithium-ion batteries. *Renew Sustain Energy Rev*. 2021;148(June):111301. doi:10.1016/j.rser.2021.111301

3. Adebanjo IT, Eko J, Agbeyegbe AG, et al. A comprehensive review of lithium-ion battery components degradation and operational considerations: a safety perspective. *Energy Adv*. 2025;4(7):820-877. doi:10.1039/d5ya00065c

4. Chung Y, Kim MS. Thermal analysis and pack level design of battery thermal management system with liquid cooling for electric vehicles. *Energy Convers Manag*. 2019;196:105-116. doi:10.1016/j.enconman.2019.05.083

5. Ki S, Lee J, Kim S, et al. An energy-efficient battery thermal management system incorporating a porous metal-based multiscale flow manifold. *Energy Convers Manag*. 2022;269. doi:10.1016/j.enconman.2022.116147

6. Al-Zareer M, Da Silva C, Amon CH. Predicting anisotropic thermophysical properties and spatially distributed heat generation rates in pouch lithium-ion batteries. *J Power Sources*. 2021;510. doi:10.1016/j.jpowsour.2021.230362

7. Al-Zareer M, Michalak A, Da Silva C, Amon CH. Predicting specific heat capacity and directional thermal conductivities of cylindrical lithium-ion batteries: A combined experimental and simulation framework. *Appl Therm Eng*. 2021;182. doi:10.1016/j.applthermaleng.2020.116075

8. Al-Zareer M, Ebbs-Picken T, Michalak A, et al. Heat generation rates and anisotropic thermophysical properties of cylindrical lithium-ion battery cells with different terminal mounting configurations. *Appl Therm Eng*. 2023;223(April 2022):119990. doi:10.1016/j.applthermaleng.2023.119990

Energy Advances Accepted Manuscript

View Article Online
DOI: 10.1039/D6YA00018E

Open Access Article. Published on 10 June 2026. Downloaded on 6/18/2026 2:09:24 PM.
This article is licensed under a Creative Commons Attribution-NonCommercial 3.0 Unported Licence.

9. Jiang Y, Huang J, Xu P, Wang P. Axial and radial thermal conductivity measurement of 18,650 Lithium-ion battery. *J Energy Storage*. 2023;72. doi:10.1016/j.est.2023.108516

10. Lin J, Chu HN, Monroe CW, Howey DA. Anisotropic Thermal Characterisation of Large-Format Lithium-Ion Pouch Cells**. *Batter Supercaps*. 2022;5(5). doi:10.1002/batt.202100401

11. Xie Y, Zheng J, Hu X, et al. An improved resistance-based thermal model for prismatic lithium-ion battery charging. *Appl Therm Eng*. 2020;180. doi:10.1016/j.applthermaleng.2020.115794

12. Akbarzadeh M, Kalogiannis T, Jaguemont J, et al. Thermal modeling of a high-energy prismatic lithium-ion battery cell and module based on a new thermal characterization methodology. *J Energy Storage*. 2020;32. doi:10.1016/j.est.2020.101707

13. Alvarez OA, Da CM, Amon CH. Multi-length-scale thermal modeling of lithium-ion batteries from sub-cell to pack. *Appl Therm Eng*. 2026;282(July 2025):128814. doi:10.1016/j.applthermaleng.2025.128814

14. Rizvi S, Tahir MW, Ramzan N, Merten C. Multiscale-multidomain model order reduction of Lithium-ion batteries for automobile application: A review. *J Energy Storage*. 2024;99(PB):113390. doi:10.1016/j.est.2024.113390

15. Perez Estevez MA, Calligaro S, Bottesi O, Caligiuri C, Renzi M. An electro-thermal model and its electrical parameters estimation procedure in a lithium-ion battery cell. *Energy*. 2021;234:121296. doi:10.1016/j.energy.2021.121296

16. Tang Y, Wu L, Wei W, et al. Study of the thermal properties during the cyclic process of lithium ion power batteries using the electrochemical-thermal coupling model. *Appl Therm Eng*. 2018;137(February):11-22. doi:10.1016/j.applthermaleng.2018.03.067

17. Wang Q kun, He Y jun, Shen J ni, Ma Z feng, Zhong G bin. A uni fi ed modeling framework for lithium-ion batteries : An arti fi cial neural network based thermal coupled equivalent circuit model approach. *Energy*. 2017;138:118-132. doi:10.1016/j.energy.2017.07.035

18. Palmieri B, Cilento F, Siviello C, Bertocchi F, Giordano M, Martone A. Mitigation of Heat Propagation in a Battery Pack by Interstitial Graphite Nanoplatelet Layer: Coupled Electrochemical-Heat Transfer Model. *J Compos Sci*. 2022;6(10). doi:10.3390/jcs6100296

19. Zhao Y, Diaz LB, Patel Y, Zhang T, Offer GJ. How to Cool Lithium Ion Batteries: Optimising Cell Design using a Thermally Coupled Model. *J Electrochem Soc*. 2019;166(13):A2849-A2859. doi:10.1149/2.0501913jes

20. Ali MA, Da Silva CM, Amon CH. Multiscale Modelling Methodologies of Lithium-Ion Battery Aging: A Review of Most Recent Developments. *Batteries*. 2023;9(9):1-37. doi:10.3390/batteries9090434

21. Wang D, Zhang Q, Huang H, Yang B, Dong H, Zhang J. An electrochemical–thermal model of lithium-ion battery and state of health estimation. *J Energy Storage*. 2022;47(August 2021):103528. doi:10.1016/j.est.2021.103528

22. Li H, Saini A, Liu C, et al. Electrochemical and thermal characteristics of prismatic lithium-ion battery based on a three-dimensional electrochemical-thermal coupled model. *J Energy Storage*. 2021;42. doi:10.1016/j.est.2021.102976

Energy Advances Accepted Manuscript

View Article Online
DOI: 10.1039/D6YA00018E

Open Access Article. Published on 10 June 2026. Downloaded on 6/18/2026 2:09:24 PM.
This article is licensed under a Creative Commons Attribution-NonCommercial 3.0 Unported Licence.

23. An Z, Jia L, Wei L, Dang C, Peng Q. Investigation on lithium-ion battery electrochemical and thermal characteristic based on electrochemical-thermal coupled model. *Appl Therm Eng*. 2018;137:792-807. doi:10.1016/j.applthermaleng.2018.04.014

24. He CX, Yue QL, Wu MC, Chen Q, Zhao TS. A 3D electrochemical-thermal coupled model for electrochemical and thermal analysis of pouch-type lithium-ion batteries. *Int J Heat Mass Transf*. 2021;181. doi:10.1016/j.ijheatmasstransfer.2021.121855

25. Lin XW, Zhou ZF, Zhu XG, et al. Non-uniform thermal characteristics investigation of three-dimensional electrochemical-thermal coupled model for pouch lithium-ion battery. *J Clean Prod*. 2023;417. doi:10.1016/j.jclepro.2023.137912

26. Samba A, Omar N, Gualous H, Capron O, Van Den Bossche P, Van Mierlo J. Impact of tab location on large format lithium-ion pouch cell based on fully coupled tree-dimensional electrochemical-thermal modeling. *Electrochim Acta*. 2014;147:319-329. doi:10.1016/j.electacta.2014.08.115

27. Moayedi H. Performance improvement and thermal management of a lithium-ion battery by optimizing tab locations and cell aspect ratio. *Int J Heat Mass Transf*. 2023;214. doi:10.1016/j.ijheatmasstransfer.2023.124456

28. Zhang X, Chang X, Shen Y, Xiang Y. Electrochemical-electrical-thermal modeling of a pouch-type lithium ion battery: An application to optimize temperature distribution. *J Energy Storage*. 2017;11:249-257. doi:10.1016/j.est.2017.03.008

29. Mastali M, Foreman E, Modjtahedi A, et al. Electrochemical-thermal modeling and experimental validation of commercial graphite/LiFePO4 pouch lithium-ion batteries. *Int J Therm Sci*. 2018;129(March):218-230. doi:10.1016/j.ijthermalsci.2018.03.004

30. Hu Y, Choe SY, Garrick TR. Measurement of two-dimensional heat generation rate of pouch type lithium-ion battery using a multifunctional calorimeter. *J Power Sources*. 2022;532. doi:10.1016/j.jpowsour.2022.231350

31. Yi J, Kim US, Shin CB, Han T, Park S. Three-Dimensional Thermal Modeling of a Lithium-Ion Battery Considering the Combined Effects of the Electrical and Thermal Contact Resistances between Current Collecting Tab and Lead Wire. *J Electrochem Soc*. 2013;160(3):A437-A443. doi:10.1149/2.039303jes

32. Taheri P, Mansouri A, Yazdanpour M, Bahrami M. Theoretical analysis of potential and current distributions in planar electrodes of lithium-ion batteries. *Electrochim Acta*. 2014;133:197-208. doi:10.1016/j.electacta.2014.04.040

33. Akhtari Zavareh P, Matam AN, Shah K. Heterogeneous Aging in a Multi-cell Lithium-ion Battery System Driven by Manufacturing-induced Variability in Electrode Microstructure: A Physics-Based Simulation Study. *Energy Adv*. Published online 2025. doi:10.1039/d5ya00182j

34. Galatro D, Al-Zareer M, Da Silva C, Romero DA, Amon CH. Thermal behavior of Lithium-ion batteries: Aging, heat generation, thermal management and failure. *Front Heat Mass Transf*. 2020;14:1-18. doi:10.5098/hmt.14.17

35. Liu Y, Tang S, Li L, et al. Simulation and parameter identification based on electrochemical-thermal coupling model of power lithium ion-battery. *J Alloys Compd*. 2020;844:156003.

Energy Advances Accepted Manuscript

View Article Online
DOI: 10.1039/D6YA00018E

doi:10.1016/j.jallcom.2020.156003

36. Li H, Saini A, Liu C, et al. Electrochemical and thermal characteristics of prismatic lithium-ion battery based on a three-dimensional electrochemical-thermal coupled model. *J Energy Storage*. 2021;42(July):102976. doi:10.1016/j.est.2021.102976

37. Li W, Cao D, Jöst D, et al. Parameter sensitivity analysis of electrochemical model-based battery management systems for lithium-ion batteries. *Appl Energy*. 2020;269(May):115104. doi:10.1016/j.apenergy.2020.115104

38. Hu Y, Choe SY, Garrick TR. Measurement of heat generation rate and heat sources of pouch type Li-ion cells. *Appl Therm Eng*. 2021;189. doi:10.1016/j.applthermaleng.2021.116709

39. Bahiraei F, Fartaj A, Nazri GA. Electrochemical-thermal Modeling to Evaluate Active Thermal Management of a Lithium-ion Battery Module. *Electrochim Acta*. 2017;254:59-71. doi:10.1016/j.electacta.2017.09.084

40. Liu Y, Tang S, Li L, et al. Simulation and parameter identification based on electrochemical-thermal coupling model of power lithium ion-battery. *J Alloys Compd*. 2020;844. doi:10.1016/j.jallcom.2020.156003

41. Li W, Cao D, Jöst D, et al. Parameter sensitivity analysis of electrochemical model-based battery management systems for lithium-ion batteries. *Appl Energy*. 2020;269. doi:10.1016/j.apenergy.2020.115104

Open Access Article. Published on 10 June 2026. Downloaded on 6/18/2026 2:09:24 PM.
This article is licensed under a Creative Commons Attribution-NonCommercial 3.0 Unported Licence.

Energy Advances Accepted Manuscript

View Article Online
DOI: 10.1039/D6YA00018E

Open Access Article. Published on 10 June 2026. Downloaded on 6/18/2026 2:09:24 PM.
This article is licensed under a Creative Commons Attribution-NonCommercial 3.0 Unported Licence.

## Manuscript

***A 3D Electrochemical-Thermal Coupled Model for Pouch-Type Lithium-ion Batteries with Counter-Tab Configuration***

## Data availability

Data will be made available on request.

Energy Advances Accepted Manuscript